Metabolic Engineering Communications 15 (2022) e00206

Contents lists available at ScienceDirect

Metabolic Engineering Communications

journal homepage: www.elsevier.com/locate/mec

Tuning a high performing multiplexed-CRISPRi *Pseudomonas putida* strain to further enhance indigoidine production

Jeffrey J. Czajka [a], Deepanwita Banerjee [b,c], Thomas Eng [b,c], Javier Menasalvas [b,c], Chunsheng Yan [b,c], Nathalie Munoz Munoz [d,e], Brenton C. Poirier [d,e], Young-Mo Kim [d,e], Scott E. Baker [d], Yinjie J. Tang [a,**], Aindrila Mukhopadhyay [b,c,f,*]

[a] *Department of Energy, Environmental and Chemical Engineering, Washington University, St. Louis, MO, 63130, USA*
[b] *Joint BioEnergy Institute, Lawrence Berkeley National Laboratory, Emeryville, CA, 94608, USA*
[c] *Biological Systems and Engineering Division, Lawrence Berkeley National Laboratory, Berkeley, CA, 94720, USA*
[d] *Earth and Biological Sciences Directorate, Pacific Northwest National Laboratory, Richland, WA, 99352, USA*
[e] *Agile BioFoundry, Emeryville, CA, 94608, USA*
[f] *Environmental Genomics and Systems Biology Division, Lawrence Berkeley National Laboratory, Berkeley, CA, 94720, USA*

ARTICLE INFO

Keywords:
Growth coupling
^{13}C-MFA
Pseudomonas putida KT2440
Multiplexed CRISPR interference
Indigoidine
Cpf1/Cas12a

ABSTRACT

In this study, a 14-gene edited *Pseudomonas putida* KT2440 strain for heterologous indigoidine production was examined using three distinct omic datasets. Transcriptomic data indicated that CRISPR/dCpf1-interference (CRISPRi) mediated multiplex repression caused global gene expression changes, implying potential undesirable changes in metabolic flux. ^{13}C-metabolic flux analysis (^{13}C-MFA) revealed that the core *P. putida* flux network after CRISPRi repression was conserved, with moderate reduction of TCA cycle and pyruvate shunt activity along with glyoxylate shunt activation during glucose catabolism. Metabolomic results identified a change in intracellular TCA metabolites and extracellular metabolite secretion profiles (sugars and succinate overflow) in the engineered strains. These omic analyses guided further strain engineering, with a random mutagenesis screen first identifying an optimal ribosome binding site (RBS) for Cpf1 that enabled stronger product-substrate pairing (1.6–fold increase). Then, deletion strains were constructed with excision of the PHA operon (Δ*phaAZC-IID*) resulting in a 2.2–fold increase in indigoidine titer over the optimized Cpf1-RBS construct at the end of the growth phase (~6 h). The maximum indigoidine titer (at 72 h) in the Δ*phaAZC-IID* strain had a 1.5–fold and 1.8–fold increase compared to the optimized Cpf1-RBS construct and the original strain, respectively. Overall, this study demonstrated that integration of omic data types is essential for understanding responses to complex metabolic engineering designs and directly quantified the effect of such modifications on central metabolism.

1. Introduction

Pseudomonas putida KT2440 is emerging as an advantageous metabolic engineering chassis due to its genetic tractability, rapid growth rate, and robust ability to grow on renewable carbon streams (Nikel and de Lorenzo, 2018). Previous efforts have targeted natural and heterologous bioproducts for production in *P. putida* including biofuels (phenazine, methyl ketones) (Askitosari et al., 2019; Dong et al., 2019), lipids (rhamnolipid) (Arnold et al., 2019), polymers (polyhydroxyalkanoate) (Yang et al., 2019), and organic acids (adipic acid) (Niu et al., 2020). Recently, *P. putida* KT2440 production of the non-ribosomal peptide indigoidine, a sustainable high-value colorant with uses in the textile, cosmetics, and dye industries, achieved promising titers of ~2 g/L in shaking flasks cultivations and ~26 g/L during fed-batch cultivations (Banerjee et al., 2020). This previous study used a genomically integrated heterologous pathway (*bpsA* and *sfp*) to catalyze the conversion of glutamine to indigoidine. In turn, a single design-build-test cycle led to improved production. The design was generated using the constrained minimal cut set (cMCS) genome-scale modeling technique which identifies genetic targets for deletion to obtain strong product-substrate

* Corresponding author. Joint BioEnergy Institute, Lawrence Berkeley National Laboratory, Emeryville, CA, 94608, USA.
** Corresponding author.
E-mail addresses: yinjie.tang@wustl.edu (Y.J. Tang), amukhopadhyay@lbl.gov (A. Mukhopadhyay).

https://doi.org/10.1016/j.mec.2022.e00206
Received 3 May 2022; Received in revised form 1 September 2022; Accepted 6 September 2022
Available online 13 September 2022

growth coupling (Klamt and Mahadevan, 2015; Trinh et al., 2009). A multiplexed CRISPR-interference (CRISPRi/dCpf1/dCas12a) system enabled simultaneous knockdown of the 14 selected gene targets (Fig. 1). The product-substrate paired strain (PSP strain) had a 30% improvement in indigoidine production and in fed-batch mode, showed growth coupled production. These advances were achieved despite the partial design implementation as verified by collected transcriptomic and proteomic data (Banerjee et al., 2020). As a highly engineered system, the PSP strain represented a valuable system to examine the effects of engineered pathways on *P. putida* and potential emergent metabolic features and phenotypes. Strains generated by these methods use complex DBTL cycles and typically contain more failure routes (e.g., multiple components or genetic circuits that can accumulate mutations detrimental to production) and may therefore struggle to achieve the large improvements obtained in initial cycles. Insight gained here on the engineered PSP strain can guide further strain designs after strain performance has already reached a relatively high production level.

^{13}C-Metabolic flux analysis (MFA) is a technique that measures intracellular enzymatic rates in different cell states and has been employed to guide strain engineering. This approach has deciphered cellular energy metabolism (He et al., 2014; You et al., 2015), flux responses to genetic perturbation (Long et al., 2016), and pathway regulations (Long and Antoniewicz, 2019a). Previous ^{13}C–MFA studies of *P. putida* metabolism during growth on glucose revealed several core metabolic features, such as the Entner-Doudoroff (ED)-EMP cycle, an active pyruvate shunt, and an inactive glyoxylate shunt (Kohlstedt and Wittmann, 2019; Nikel et al., 2015, 2021). While these foundational metabolic features have been clearly established, the metabolic rewiring of *P. putida* strains in response to complex engineering of central pathways is unknown. Many studies in microbes have examined flux changes in response to simple genetic edits (*i.e.,* deletion or overexpression (He et al., 2019; Long and Antoniewicz, 2019b; Long et al., 2016; Xu et al., 2021), however the impact of transcriptional downregulation due to multiplexed CRISPRi on flux topology has not been examined in-depth in any microbe. Due to the complexity and technical challenges needed to accurately quantify metabolic flux, previous researchers have used gene expression analysis (RNAseq) as a proxy in these engineered strains (Reis et al., 2019; Silvis et al., 2021; Zhao et al., 2019). The indigoidine producing *P. putida* strains were an ideal system to investigate as both a case study of the response of *P. putida* network to genetic manipulation and CRISPRi downregulation as production was previously characterized in a minimal defined medium compatible with ^{13}C-MFA (Banerjee et al., 2020) and as global changes were observed from transcriptomics data.

Here, metabolic responses of *P. putida* to multiplex CRISPRi gene knockdown were characterized by direct flux measurements, which revealed overall pathway responses and functions. Targeted metabolite analysis helped identify congestion nodes in the flux network. By integrating metabolomic and flux data with previously collected transcriptomic information, prominent gene deletion targets for improved production were rationally selected and experimentally tested in new deletion strains generated via ssDNA recombineering.

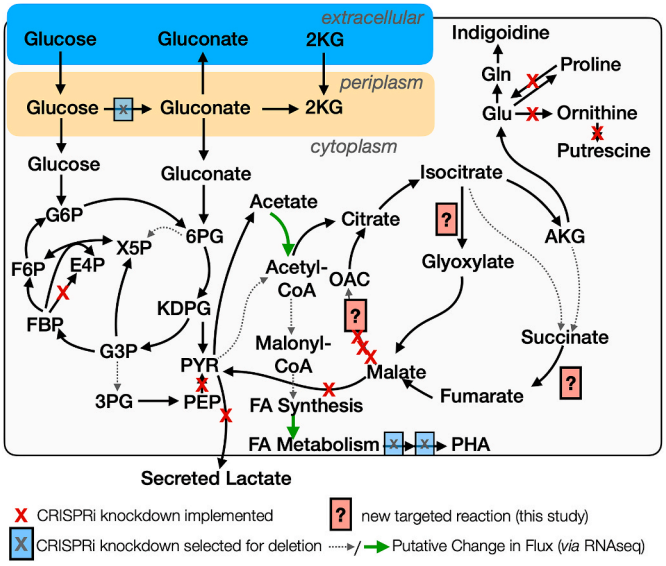

Fig. 1. Analysis of *P. putida* PSP Rewired Central Metabolism from Transcriptomics and Proteomics. Central metabolism of the Product Substrate Paired (PSP) *P. putida* strain which produced indigoidine from glucose was analyzed by RNAseq and targeted proteomics. Genes targeted for knockdown by CRISPRi/dCpf1 which showed at least 30% reduction in RNA and protein levels are indicated by red X marks, and unsuccessful knockdown gene targets are indicated with blue X marks. Not all of the gene targets outside of central metabolism were depicted in the figure (Banerjee et al., 2020). This subset of CRISPRi targets were in turn selected for gene deletion in this study. Potential rate-limiting metabolic reactions rationally identified by omics analysis are highlighted with red question marks (?). Differential RNA expression levels in the PSP strain at the 24 h time point compared to 0 h time point were mapped to their corresponding metabolic reactions. Thin grey dashed lines indicate at least a 4-fold (log2<−2) decrease in RNA levels, and thick green lines indicate at least a 4-fold (log2>2) increase in RNA levels, as a proxy for metabolic flux. Refer to Supplementary Table S3 and Supplementary **DataFile 1** for the complete RNAseq dataset for definitions and list of abbreviations within the Supplementary Material. (For interpretation of the references to color in this figure legend, the reader is referred to the Web version of this article.)

2. Materials and Methods

2.1. Strains and plasmids

All strains used in this study are listed in Table 1. The strains analyzed via ^{13}C–MFA were the wild type (WT), the strain containing engineered indigoidine production pathway (Eng), and the strain containing both the engineered indigoidine production pathway and the CRISPRi product-substrate pairing plasmid (PSP) (Fig. 1).

Expression of the heterologous indigoidine pathway is under the control of an arabinose inducible promoter (Banerjee et al., 2020). The PSP strain gRNA expression cassette is induced by adding IPTG. The gRNA targeted 14 genes for downregulation (*gcd, tal, lldp, ppsA, maeB, mdh, mqo-II, mqo-II, putA, argE, speC, anmK, phaA, phaC-II*). All plasmids contain *neo* which confers resistance to kanamycin for selection. *dcpf1* is the endonuclease de-activated allele of *Francisella novicida U112 cpf1* (Cpf1-D917N). The endonuclease active allele is referred to as *acpf1*. The sequences of the plasmids generated in this study may be visualized at public-registry.jbei.org.

2.2. Chemicals and growth medium

Labeled substrates [1,2–^{13}C glucose, 6–^{13}C glucose, 1–^{13}C glucose, U–$^{13}C_6$ glucose] were purchased from Omicron Biochemicals (South Bend, IN) or Sigma-Aldrich (St. Louis, MO). All other chemicals were purchased from Sigma-Aldrich. *P. putida* strains were grown in LB medium or M9 minimal medium [per liter, 2 g $(NH_4)_2SO_4$, 6.8 g Na_2HPO_4, 3 g KH_2PO_4, 0.5 g NaCl, 1 mL trace elements solution (Teknova, Hollister, CA), 100 μL 1 M $CaCl_2$, 2 mL 1 M $MgSO_4$] supplemented with 10 g/L of glucose. Arabinose (3 g/L), IPTG (0.5 mM), and kanamycin (50 μg/L) were added as necessary for indigoidine production and were included at inoculation.

2.3. Cell cultivation

P. putida cultivated for metabolomic and fluxomic analyses were grown in 14 mL of liquid volume in 50 mL unbaffled shaking flasks at 30 °C and 200 rpm. Seed cultures were inoculated from fresh plates (<3 days old) in 5 mL of LB medium and grown overnight. A 1.4%

Table 1
Strains and plasmids used in this study.

Strain annotation	Strain	Source
WT	*P. putida* KT2440	(Banerjee et al., 2020; Nieto et al., 1990)
Eng strain[a]	KT2440 *PP_5402::arap-Sc.bpsA,Bc.sfp*	(Banerjee et al., 2020); JBEI-137,184
PSP strain[a]	KT2440 *PP_5402::arap-Sc.bpsA,Bc.sfp* {p/pTE327 *neo BBR1 lacuv5p-dcpf1* 14 gene CRISPRi array}	(Banerjee et al., 2020); JBEI-105,555
pTE442 strain[a]	KT2440 *PP_5402::arap-Sc.bpsA,Bc.sfp* {p/pTE442 *neo BBR1 lacuv5p-dcpf1* 14 gene CRISPRi array dcpf1-RBS optimized sequence}	This study JBEI-230,534
Δ4116[a]	KT2440 ΔPP_4116 *PP_5402::arap-Sc.bpsA, Bc.sfp* {p/pTE442 *neo BBR1 lacuv5p-dcpf1* 14 gene CRISPRi array dcpf1-RBS optimized sequence}	This study JBEI-230,533
Δ4185 Δ4186[a]	KT2440 ΔPP_4185 ΔPP_4186 *PP_5402:: arap-Sc.bpsA,Bc.sfp* {p/pTE442 *neo BBR1 lacuv5p-dcpf1* 14 gene CRISPRi array optimized dcpf1-RBS optimized sequence}	This study JBEI-230,532
Δ0751[a]	KT2440 ΔPP_0751 *PP_5402::arap-Sc.bpsA, Bc.sfp* {p/pTE442 *neo BBR1 lacuv5p-dcpf1* 14 gene CRISPRi array dcpf1-RBS optimized sequence}	This study JBEI-230,531
ΔphaAZC-IID[a]	KT2440 Δ*phaAZC-IID* (ΔPP_5003 ΔPP_5004 ΔPP_5005 ΔPP_5006) *PP_5402:: arap-Sc.bpsA,Bc.sfp* {p/pTE442 *neo BBR1 lacuv5p-dcpf1* 14 gene CRISPRi array dcpf1-RBS optimized sequence}	This study JBEI-230,530
Δ*pyrF*	KT2440 Δ*pyrF* (ΔPP_1815)	This study; JBEI-204,817

Plasmid name	Miscellaneous Notes; gRNA Targets	Source
pTE219	*lacMp-dcpf1; gRNA*-PmeI. Control plasmid; gRNA targets a randomly-generated 20 nt sequence + PmeI cut site absent from the *P. putida* genome	(Banerjee et al., 2020)
pTE327	*lacMp-dcpf1; gcd, tal, lldp, ppsA, maeB, mdh, mqo-II, mqo-II, putA, argE, speC, anmK, phaA, phaC-II*	(Banerjee et al., 2020)
pTE442	*lacMp-RBSopt-dcpf1*; *gcd, tal, lldp, ppsA, maeB, mdh, mqo-II, mqo-II, putA, argE, speC, anmK, phaA, phaC-II*	This study; JBEI-204,831
pAO1 (pTE452)	pORTMAGE-Pa1 *pmp-Pa.recT,Pa.mutL-E36K BBR1* GmR 3-methyl-benzoate inducible promoter.	(Wannier et al., 2020)
pTE355	*lacMp-acpf1 neo BBR1 gRNA-PP_1815* for RBS-*aCpf1* mutagenesis	This study; JBEI-204,819
pTE469	*lacMp-RBSopt-acpf1 neo BBR1 gRNA-PP_0751* for recombineering	This study; JBEI-204,820
pTE486	*lacMp-RBSopt-acpf1 neo BBR1 gRNA-PP_1444* for recombineering	This study; JBEI-204,823
pTE504	*lacMp-RBSopt-acpf1 neo BBR1 gRNA-PP_5003* for recombineering	This study; JBEI-204,825
pTE505	*lacMp-RBSopt-acpf1 neo BBR1 gRNA-PP_4186* for recombineering	This study; JBEI-204,827
pTE506	*lacMp-RBSopt-acpf1 neo BBR1 gRNA-PP_4116* for recombineering	This study; JBEI-204,829

[a] Genomic integrations are targeted to an intergenic region adjacent to the indicated locus.

inoculation ratio was used to start 14 mL liquid cultures of M9 minimal medium. Cells from these first M9 minimal medium cultures were harvested around 8–12 h after inoculation (OD_{600} = ~2–5) and subcultured in M9 production medium at an initial OD_{600} of 0.06–0.10. Samples for the metabolomic, fluxomic, and production assay experiments were collected from the subculture. Fluxomic experiments substituted the unlabeled glucose in the subculture with either 1,2–^{13}C glucose, a 80:20 mixture of 6–^{13}C glucose:U–$^{13}C_6$ glucose or a 80:20 mixture of 1–^{13}C glucose:U–$^{13}C_6$ glucose (Cambridge Isotope, MA and Omicron Biochemicals, IN). Cultures used as internal standards for metabolomic measurements were grown in two subsequent M9 media cultures containing 100% U–$^{13}C_6$ glucose.

2.4. Dry cell weight measurements

The dry cell weight per OD_{600} measurements were collected from cultures grown with M9 minimal media (1st subculture). Cells were inoculated to an approximate OD_{600} of 0.06 in 50 mL of M9 minimal media in 250 unbaffled shaking flasks. OD_{600} was measured throughout the growth with biological replicates harvested at various OD_{600} values via centrifugation at 5000×*g* for 10 min. The supernatant was then discarded, the pellet washed with 0.9% NaCl, and the liquid re-centrifuged. Samples were frozen at −80 °C before lyophilization and measurement. One OD_{600} unit was 0.37 ± 0.02 g/L biomass at the end of the growth phase (Fig. S1).

2.5. Sample collection and processing for metabolomic analysis

Metabolomic samples were collected at both the growth phase (OD_{600} range of 0.8–1) and the production phase (24 h, OD_{600} range of 8–10). The sampling process involved rapidly quenching metabolism using a carbon-free media in a liquid nitrogen bath. Specifically, the culture was poured into a chilled (~0 °C) M9 media solution that was rapidly stirred in a liquid nitrogen bath until the culture reached ~0 °C. Cells were then pelleted at 5000×*g* for 5 min (at 1 °C), flash frozen with liquid nitrogen, and stored at −80 °C until metabolite extractions were performed. Intracellular metabolites were extracted in a 1 mL 7:3 MeOH:Chloroform solution at 4 °C, and then processed and analyzed as previously described (Czajka et al., 2020a). Intracellular concentrations were normalized via the dry cell weight correlations (Fig. S1). An isotopic labeling ratio method was used to determine relative metabolite intracellular concentrations across cultures as previously described (Abernathy et al., 2017). Briefly, *P. putida* cells were grown in 100% U–$^{13}C_6$ M9 minimal media in (50 mL of media in 250 mL shaking flasks) for two subcultures (see **Methods section 2.3**). Cells were harvested during the mid-exponential phase using the liquid nitrogen bath described above. Labeled biomass was mixed with the labeled cells in a known quantity before metabolite extraction and Liquid Chromatography-Mass Spectroscopy (LC-MS) measurements. The labeled to unlabeled isotopic ratio percentage of each metabolite was used to obtain relative measurements. Cultivation media was filtered through 0.2 μm sterile filters and lyophilized for extracellular metabolite measurements using the same method. A second set of extracellular metabolites were quantified from 20 μl of spent media that were dried under vacuum. Chemical derivatization, analysis by GC-MS (same instrument as citation), and data processing was done as previously described (Pomraning et al., 2021). Glucose content was determined via enzymatic kit (R-Biopharm, Darmstadt, Germany) per manufacturer's instructions.

2.6. Sample collection and processing for proteinogenic measurements

Proteinogenic amino acid label incorporation samples were harvested from cultures that were grown to an OD_{600} range of 0.7–1.1. Cells were pelleted at 5000×*g* for 5 min, the supernatant was discarded, and the pellet was frozen at −80 °C until processing. Proteins from cultures grown with 1–^{13}C or 6–^{13}C glucose were collected from a MPLEx extraction protocol (Nakayasu et al., 2016), hydrolyzed with 6 N HCl at 100 °C for 20 h and dried with a speed vacuum concentrator. The amino acids were then dissolved in 20 μL of pure pyridine and chemically derivatized using 80 μL of tert-butyldimethylsilyl trifluoromethanesulfonate (TBDMS) at 70 °C for 1 h. The raw data were analyzed and amino acid fragments were corrected for natural labeling abundance by the software DExSI (Dagley and McConville, 2018). All other samples were hydrolyzed with 1 mL of 6 N HCl at 100 °C for 20 h,

dried with filtered air, and derivatized using 100 μL of TBDMS in 100 μL of THF at 70 °C for 1 h. All amino acid derivatized samples were analyzed via GC-MS equipped with a HP-5MS column as previously described (Hollinshead et al., 2019). The amino acid fragments were corrected for natural labeling abundance according to the published method (Wahl et al., 2004).

2.7. Indigoidine and glucose measurements

Indigoidine production and quantification was performed as previously described with slight modifications (Banerjee et al., 2020). Briefly, either 500 μL (OD_{600} = 1) or 100 μL (24 h, 48 h samples) of liquid culture was pelleted at 24,000×*g* for 2 min. The supernatant was discarded, and 500 μL of dimethylsulfoxide (DMSO) was used to resuspend and extract the indigoidine via vortexing (10 min). Additional DMSO was added if the pellet was not fully dissolved. Absorption was measured at 612 nm in a Cary 60 UV–Vis Spectrometer (Agilent Technologies). The values here were reported as absorbance, but can be converted to absolute concentration (g/L) using a previously determined calibration curve (Banerjee et al., 2020).

2.8. Flux modeling

A core *P. putida* metabolic network was constructed from published resources (Kohlstedt and Wittmann, 2019). Only the periplasmic secretion reactions were included in the model as small metabolite labeling was needed to distinguish flux from the gluconate node to central metabolism (Table S1). The INCA software package was used to analyze the metabolic network (Young, 2014) for parallel tracer experiments. The WUflux software was employed to cross-validate the flux calculations using the 1,2–^{13}C glucose derived data (He et al., 2016). The indigoidine production rates and secretion rates constrained the network to represent MFA models for each of the three strains. The glucose depletion measurements and biomass formation at 6 h along with initial glucose and biomass concentrations were used to calculate the uptake per biomass yield and to evaluate the models (Fig. S2). The 6 h measurements correspond to the growth phase, and therefore, the MFA models are designed to represent the growth phase and not necessarily the production phase. The amino acid requirements for the biomass equation were obtained from the *P. putida* genome-scale metabolic model iJN1462 (Nogales et al., 2020). The central carbon metabolite precursors required for sugar and lipid production (Acetyl-CoA, G6P, F6P, GAP) were obtained from a metabolite only biomass equation that was reported and determined in a previous flux analysis study of *P. putida* KT2440 (Kohlstedt and Wittmann, 2019). The network transitions and constraints can be found in Table S1 and are also included in the provided supplementary INCA models. The chi-squared goodness of fit method, which assumes that the minimized variance-weighted sum of squared residuals (SSR) follows a chi-square distribution, was used to assess the confidence of flux best fits at 95% confidence interval (Young, 2014).

2.9. Identification of an optimized RBS sequence for Cpf1 function

A small library of ribosome binding site variants for *Francisella novicida U112 cpf1* were calculated using denovoDNA (Salis et al., 2009) and incorporated into a plasmid containing an endonuclease active (D917) allele of *cpf1* and a gRNA targeting *pyrF* (PP_1815) using site directed mutagenesis (Deng and Nickoloff, 1992) with Q5 polymerase (NEB). The RBS mutant library was encoded by the degenerate sequence 5′-GYAGAASAKTCMAAATGGKGASRTGGAT-3'. The library was transformed into *E. coli* DH10-beta competent cells (NEB); approximately 50 single colonies were picked, inoculated into liquid LB media with 50 μg/mL kanamycin, and single plasmids were extracted using a Miniprep plasmid DNA extraction kit (Qiagen Research, Germantown, MA). *P. putida* KT2440 and the Δ*pyrF* strain were made electrocompetent (Wang et al., 2009) and transformed with a variant plasmid from the RBS library. Following an hour outgrowth in LB media at 30 °C (200 rpm shaking), the entirety of the transformation was spun down and plated on an LB kanamycin plate and incubated at 30 °C overnight. Candidate RBS-variant *acpf1* plasmids were identified by the following criteria: >200 CFU/μg plasmid DNA in the Δ*pyrF* strain background; <5 CFU/μg plasmid DNA in the KT2440 wild-type background. One candidate clone, RBS isolate number 30, met this criterion. The RBS sequence was identified by Sanger sequencing and corresponded to the following sequence identity: 5′-GCAGAACAGTCAAAATGGGGACGTGGAT-3'. This RBS sequence was introduced into the multiplex CRISPRi/dCpf1 plasmid pTE327 using site directed mutagenesis between the J2113 promoter and start codon of *cpf1* and subsequently was given the accession ID pTE442.

2.10. Generation of deletion strains via recombineering & Cpf1/CRISPR selection

Deletion mutants were generated using a RecT-family recombinase following a modified protocol based on (Aparicio et al., 2020). Briefly, fresh transformants harboring pTE452/pAO1 were selected using LB agar plates supplemented with 30 μg/mL gentamicin. Single colonies from fresh plates (<5 days old) were used to inoculate LB gentamicin liquid cultures and grown overnight at 30 °C (200 rpm shaking). 2.5 mL of the overnight culture (OD_{600} = ~4) was used to inoculate 25 mL of fresh LB gentamicin medium in a 250 mL baffled shaking flask and grown for 1 h at 30 °C and 200 rpm. Recombinase expression was then induced with 1 mM 3-methyl-benzoate (Sigma: T36609; M-Toluic Acid 99% purity). Cells were incubated for 30 min after induction with shaking, decanted into a 50 mL falcon tube, and centrifuged for 5 min at 3000×*g* at 4 °C. The cell pellet was resuspended with 10% glycerol and transferred into an Eppendorf tube, washed with glycerol three additional times, and resuspended in 1 mL of 10% glycerol.

For each recombineering event, 50 μL of the aliquoted cells were mixed with 1 μL of the single stranded oligonucleotide (2 μM final concentration) (Table S2) and 50 ng of the appropriate cpf1-gRNA (endonuclease active) plasmid (Table 1). The above-mentioned components were electroporated into *P. putida* using 2 mm-gap cuvettes and the Bio-Rad MicroPulser (program EC2 - 2.5 kV). After pulsing, cells were immediately recovered in 600 μL of Terrific Broth (TB) and incubated for 3 h at 30 °C, 1000 rpm in a bench-top thermomixer (Eppendorf Inc, Infield, CT, USA). After outgrowth, 250 μL was plated on solid agar LB kanamycin plates for 1–3 days at 30 °C. Colonies were visible after 48 h. 8–30 clones were selected for genotyping by colony PCR using NEB OneTaq Quick-Load 2X Master Mix with Standard Buffer (catalog #M0486L) following the manufacturer's protocol. Before PCR, colony biomass was boiled at 94 °C for 45 min in 50 μL 20 mM NaOH. 2 μL of the boiled solution was used in a 25 μL PCR reaction. The annealing temperature was calculated using the webtool, NEB Tm calculator (tmcalculator.neb.com, New England Biolabs, Ipswitch, MA). The loci targeted for deletion were genotyped using colony PCR with primers that bind to the 5′ upstream and 3′ downstream regions adjacent to the targeted open reading frame (Table S2). PCR products were analyzed using standard techniques for agarose gel electrophoresis. After genotyping, both the recombineering plasmid and CRISPR plasmid were cured from the mutant by allowing random segregation; sensitivity to both kanamycin and gentamicin was verified by patching clones to solid agar media containing either of the two named antibiotics.

3. Results

The goal of this study was to integrate complementary omics analyses to "learn" where additional metabolic changes could further enhance indigoidine production. Differential gene expression from the RNAseq transcriptomics dataset of the PSP strain from Banerjee and Eng *et al* was analyzed to understand how global gene expression changes

impacted central metabolism (Fig. 1, Table S3, **Supplementary Data-File 1** (Banerjee et al., 2020)). This analysis indicated that while the dataset contained many differentially expressed genes, few of them were mappable to central metabolic reactions. A small number of transcripts from central metabolic genes were downregulated, which were likely related to the genes targeted for downregulation by CRISPRi. A notable exception was a statistically significant upregulation in beta-oxidation fatty acid metabolism associated genes related to PHA biosynthesis and genes associated with the catalytic conversion of acetate to acetyl-CoA. Since it was unclear how these changes affected the central metabolic reaction network, direct evidence of metabolic flux was desired to corroborate the RNAseq dataset.

3.1. *Unexpected metabolite overflow observed in the PSP strain stationary phase*

The first step in performing ^{13}C–MFA was to evaluate the cell physiological state under the desired cultivation conditions (M9 minimal media containing 10 g/L glucose and 2 g/L $(NH_4)_2SO_4$). It was reported that the strain containing the production pathway and the CRISPRi growth-coupling plasmid (PSP strain, Table 1) maintained a desirable phenotype under a variety of scales (deep-well microplates, shaking flasks, and bioreactors) (Banerjee et al., 2020). To minimize labeled substrate use, the culture volume was scaled down to a 14 mL fill volume in 50 mL unbaffled shaking flasks (Fig. S2a). The growth rates of the three strains in 14 mL cultures across the cultures were not statistically different (Fig. 2a–b), although there was a longer lag phase for the PSP strain due to the addition of antibiotics necessary to retain the CRISPRi plasmid (Fig. S3). This increased lag did not cause a decrease in the biomass yield coefficient of the PSP strain, as there was a corresponding decrease in glucose depletion rate (Fig. S2b), with yield coefficients in the physiological range of previous reports (del Castillo et al., 2007; Kohlstedt and Wittmann, 2019) (0.45 ± 0.02 g biomass/g glucose and 0.44 ± 0.04 g biomass/g glucose consumed for the Eng and PSP strains, respectively, see **Supplementary Methods**). The PSP strain showed a ~11% increase in production compared to the Eng strain across several runs in the 14 mL format (Fig. 2c), consistent with previously reported titers (Banerjee et al., 2020).

The next step was to determine the extracellular metabolite secretion rates to constrain the MFA model during the growth phase (≤6 h), and to determine the effects of indigoidine production and the changes in gene expression in the PSP strain on the secretion profiles. Beyond the genes in central metabolism described in Fig. 1, downregulation of 167 genes and upregulation of 139 genes were observed as an indirect consequence of the multiplex CRISPRi gene targeting (Table 1, Table S3, Fig. S4, Supplemental DataFile 1). *Pseudomonads* preferentially oxidize glucose to gluconate and 2-ketogluconate (2 KG) in the periplasm under excess glucose conditions, as opposed to direct glucose uptake and phosphorylation (Fig. 1). Both gluconate and 2 KG have been previously reported be secreted during growth on glucose minimal media (del Castillo et al., 2007; Kohlstedt and Wittmann, 2019; Nikel et al., 2021, 2015) or complex LB media (Molina et al., 2019a, 2019b). An analysis of the extracellular media revealed that both compounds were secreted towards the end of the growth phase (~6 h) in all three strains (Fig. 3a). The Eng strain secreted the highest amount, with a total of 1.4 ± 0.2 g/L (compared to 1.0 ± 0.1 g/L for the WT strain). Expression of the CRISPRi construct led to a reduction in secretion compared to both the Eng and WT strains (0.7 ± 0.1 g/L), with a 1.5–fold reduction in secretion observed when comparing values normalized to the glucose depletion rates (Fig. S2) or the growth rates. The lowered secretion indicated that the targeted knockdown of PP_1444 was successful in reducing periplasmic oxidation rates (Fig. 1) and likely contributed to the increased indigoidine production during fed-batch mode reported in the original PSP strain (Banerjee et al., 2020). An interesting observation here was that 2 KG was secreted in higher quantities than gluconate under the cultivation conditions tested (Fig. 3a). A recent study demonstrated that *P. putida* 2 KG secretion is dependent on oxygen, with higher amounts of 2 KG produced in the presence of oxygen (Pedersen et al., 2021). The WT and Eng strains secreted 2.6– and 2.9– fold more 2 KG than gluconate, while expression of the CRISPRi construct successfully reduced the amount of secreted compounds and shifted the excretion to a 1.3–fold ratio. Both compounds were re-consumed by the 24 h mark, with the exception of a small amount of residual gluconate in the PSP strain (Fig. 3b). Several minor byproducts were present in all strains (Fig. S5).

Further analysis revealed that only the PSP strain accumulated succinate as a byproduct, with 240 ± 40 mg/L detected in the production phase (Fig. 3c). The previous cMCS-based modeling (Banerjee et al., 2020) used for designing the PSP strain had not assumed an overflow of succinate, as *P. putida* succinate secretion was previously reported only under nitrogen-limiting conditions during growth on glycerol (Beckers et al., 2016). As the modeling predicted succinate to be an incompatible substrate for production (i.e., succinate would not be sufficient as a carbon source to generate precursors for both biomass growth and indigoidine production ((Banerjee et al., 2020), Fig. S6)), the flow of carbon through this node represented a potential loss of carbon from the system. The availability of succinate in the media of the PSP strain could have potentially altered the observed secretion dynamics. Therefore, succinate was added to cultivations of the Eng strain (3 g/L) at either 6 h or 24 h to verify the modeling prediction. The additional carbon led to increased biomass accumulation but not increased indigoidine levels (Fig. 3d), supporting the prediction that succinate would not be directed towards product synthesis and may represent an inefficient loss of

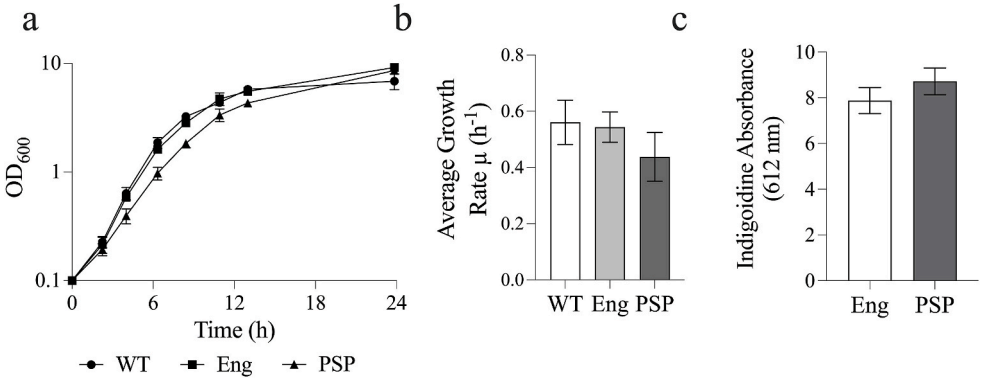

Fig. 2. Growth characterization of wild-type *P. putida* and indigoidine producing strains. (a) Growth curves (log scale) on glucose in M9 minimal medium (n = 4). Growth phase was defined as occurring up to ~6 h and production phase occurred after 6 h. Growth rates were similar between all strains after 3 h. (b) Average growth rates up to time of harvest in labeling and metabolomic experiments (n = 14). Error bars represent the standard error. (c) Indigoidine production at 48 h (n = 9). The indigoidine absorbance for the PSP strain is ~1.8 ± 0.3 g/L using a previously reported standard curve (**Methods Section 2.7** (Banerjee et al., 2020)). All measurements were from cultures grown in 14 mL volume in 50 mL shaking flasks and production medium (10 g/L glucose, 3 g/L arabinose, 2 g/L $(NH_4)_2SO_4$, 0.5 mM IPTG at time of induction. The PSP strain growth medium also contained 50 μg/L of kanamycin). Error bars represent the standard error.

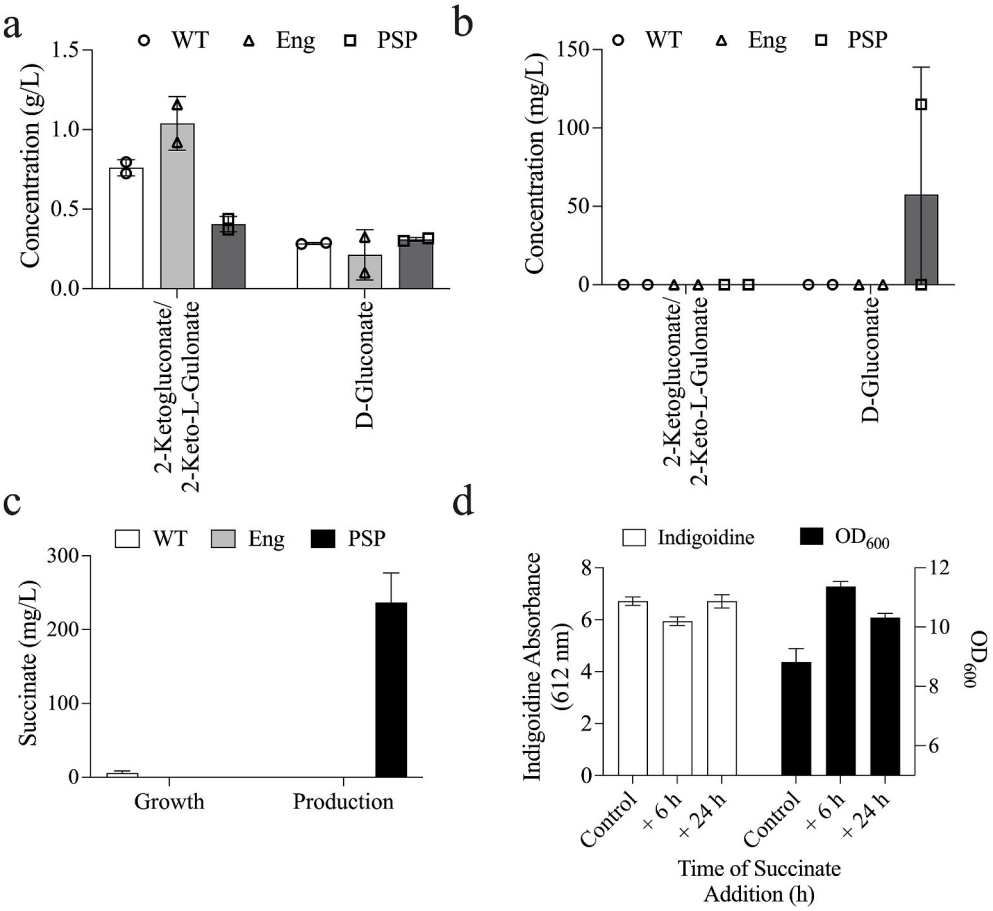

Fig. 3. Metabolite overflow and indigoidine production dynamics in the presence of succinate. (a) Secreted extracellular sugars measured at the end of the growth phase. (b) Extracellular sugars during the production phase. (c) Succinate overflow measured at the end of growth (6 h) and during production (24 h) phases. (d) Indigoidine production after succinate addition at either 6 h or 24 h after inoculation. The indigoidine absorbance for the control is ~1.4 ± 0.1 g/L using a previously reported standard curve (**see Methods Section 2.7** (Banerjee et al., 2020)). All measurements were from cultures grown in 14 mL volume in 50 mL shaking flasks and production medium (10 g/L glucose, 2 g/L $(NH_4)_2SO_4$, 3 g/L arabinose, 0.5 mM IPTG at time of induction. The PSP strain growth medium also contained 50 μg/L of kanamycin) Error bars represent the standard error (a & b, n = 2; c, n = 3; d, n = 4 (control), n = 3 (6 h and 24 h time points).

carbon. To more fully characterize cellular flux, ^{13}C-MFA was performed with isotopically labeled glucose as a tracer.

3.2. *Steady-state ^{13}C–MFA data collection and modeling*

Parallel ^{13}C–MFA tracer experiments were performed using three different labeled glucose mixtures as the carbon source (each tracer was used in an independent culture, **Methods Section 2.3**). At least three doublings of growth were allowed to occur in the labeled medium after inoculation before biomass was harvested (Wiechert et al., 2007). Steady-state flux fitting requires an assumption of metabolic and isotopic steady-state. The assumption was verified by growing the cells on a mixture of labeled glucose substrates and harvesting the biomass at different points within the desired range of growth. The resulting amino acid labeling experiment profiles were similar, with only small, non-significant differences (p-values <0.05, student's t-test) observed between timepoints (Fig. S7). This verification provided confidence to proceed with sample collection for ^{13}C-MFA.

The glucose depletion rates (6.0 ± 0.9 mmol/h, 6.6 ± 0.4 mmol/h, and 5.6 ± 1.0 mmol/h) and specific depletion rates (8.9, 8.2, and 7.8 mmol/gDCW/h) were determined for the WT, Eng, and PSP strains, respectively (Fig. S2). The fluxes were simulated by normalizing the specific glucose depletion as 100 mmol/gDCW/h, allowing for direct comparisons of the relative flux (absolute flux values were included in Tables S4–S6. The resulting fit goodness-of-fits for fragments were described in Fig. S8 and Tables S7–S9). A good quality of fit was achieved for each strain with SSR values equal to 180, 157, and 148 for the WT, Eng, and PSP strains respectively. These reported SSR values were within the expected range (from 147 to 221, from 141 to 215, and from 144 to 218 for the WT, Eng, and PSP strains, respectively), passing the chi-square test at 95% confidence levels. The ^{13}C–MFA quantified flux results represented the cell growth phase (6 h) and indicated the conservation of the core *P. putida* metabolic features within all three strains (based on features previously reported (Kohlstedt and Wittmann, 2019; Nikel et al., 2021), Fig. 4, Tables S2–S4). Namely, the ED pathway was predicted to be the exclusive catabolic route during growth on glucose, carbon reflux was observed through the cyclic ED-EMP pathway, and the pyruvate shunt was active. The largest difference between the strains was the increased cofactor production through the periplasmic oxidized reactions. In general, there were not large changes in the flux topology between the two strains which shows that the native flux network accommodates indigoidine production without resulting in significant central carbon flux changes.

On the other hand, expression of the CRISPRi system impacted the flux network of the PSP strain, with flux rewiring observed in the lower half of metabolism (i.e., the TCA cycle, pyruvate shunt, Fig. 4). CRISPRi targeting of the malic enzyme (*maeB*/PP_5085) achieved a 50% reduction in reaction flux in the PSP strain. There was a corresponding 1.3–fold decrease in the second reaction (pyruvate carboxylase) of the pyruvate shunt which agreed with observed changes in transcriptomic and proteomic levels (Banerjee et al., 2020), Table 1, Fig. S4). The malate dehydrogenase reaction (MAL → OAC) had a 1.4–fold increase in flux despite the targeted downregulation of three of the four *P. putida* malate dehydrogenase genes (*mdh*, *mqo-I*, *mqo-II*), which may be due to the activity of the untargeted *mqo-III* gene. The rearrangement of flux activity downstream of MAL propagated through the TCA cycle and resulted in approximately 1.3–fold reduction in flux from ICIT→AKG→SUC (Fig. 4, Tables S4–S5) and the activation of the glyoxylate shunt. The glyoxylate shunt pathway can allow cells to bypass bottlenecks in the TCA cycle and reduce CO_2 carbon loss. In general, the glyoxylate shunt is inactive during glucose catabolism and its activation was not predicted by the cMCS design (**Supplementary DataFile 2**

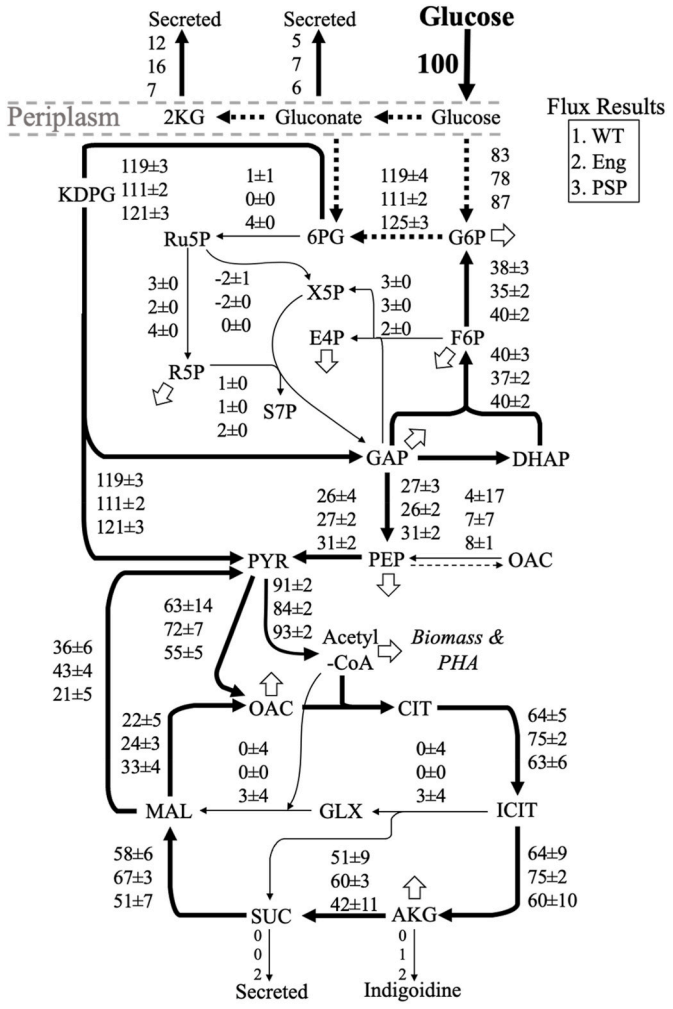

Fig. 4. Flux networks of *P. putida* strains. Flux fitting results for the three *P. putida* strains are represented using three rows, the WT (top), Eng (middle), and PSP (bottom). Hollow arrows represent metabolite drainage for biomass equations. The dashed arrow from PEP to OAC represents no predicted flux going through the reactions. Dotted lines represent reactions that were not distinguishable from proteinogenic amnio acid labeling and thus, undetermined in this network. Some reactions that do not contribute to the main points drawn from the flux maps are omitted from the figure for clarity. All reaction fits, uptake rates, and biomass formations can be found in Tables S4–S6. Flux is reported as a percentage of the glucose depletion rate, which has been normalized to 100 and was 6.0 ± 0.9 mmol/h, 6.6 ± 0.4 mmol/h, and 5.6 ± 1.0 mmol/h for the WT, Eng, and PSP strains, respectively. Goodness-of-fits of amino acid fragments can be found in Fig. S8 and Tables S7–S9. The SSR values were within the expected ranges for each strain (WT 180 [147,221], Eng 157 [141,215], PSP 148 [144,218]). For metabolite abbreviations, refer to the list of abbreviations within the Supplementary Material.

(Banerjee et al., 2020),). Recent metabolic modeling indicated that preventing PHA formation can lead to glyoxylate shunt activation in *P. putida* (Manoli et al., 2022). There was a slight (1.1–fold) increase in ED glycolysis flux but major flux rewiring was not found in the cyclic ED-EMP pathway steps. Relatively more PP pathway flux activity in the PSP strain was observed, with the carbon being directed towards further NADPH production through the first oxidative step of the PP pathway. Cofactor and ATP generation were similar between strains, with an ~10% increase of ATP generation and a 10% decrease in NADPH and NADH generation in the PSP strain relative to the Eng strain (determined from all non-amino acid forming reactions, Table S10). Overall, these flux maps revealed the effects of multiplexed CRISPRi on pathway activities were dominated by a few gene targets.

3.3. Intracellular metabolite concentration measurements

Intracellular metabolite concentrations affect the thermodynamic driving force of enzyme reactions and buffer the flux network (Raamsdonk et al., 2001). When an enzyme abundance is altered after genetic modification, the accumulation or depletion of a metabolite can help a cell maintain its flux network. Therefore, a targeted metabolomics approach was utilized to examine the intracellular metabolite concentrations (pool sizes) in the strains. The measurements revealed a shift in pool sizes between the strains at both the growth (Fig. 5a) and production phase (Fig. 5b). In the growth phase, the Eng strain was observed to have a depletion in many central carbon metabolites compared to the WT strain. Expression of the CRISPRi knockdown construct appeared to restore metabolite pool sizes to the WT level. Thus, the PSP strain had elevated metabolite pool sizes compared to the Eng strain, which may provide flux buffering and allow for improved production (Raamsdonk et al., 2001; Wegner et al., 2015). A significant difference (p-value < 0.05) of pool sizes were observed for erythrose 4-phosphate (E4P) with an approximate 2–fold increase in both the Eng and PSP engineered strains compared to the WT. There was also a significant increase of glyceraldehyde 3-phosphate (GAP) pool size (1.8–fold) in the PSP strain compared to both the WT and Eng strain. In the TCA cycle, the citrate (CIT) pool size of the PSP strain was increased by 1.7–fold and approximately 3.5–fold relative to the WT and Eng strains, respectively. There was a 2.2–fold and 2.9–fold increase of detected MAL and AKG in the PSP strain compared to the Eng strain (Fig. 5a and Fig. S9). While the reason for the E4P increase in the Eng and PSP strains remained unclear, the depletion of CIT in the Eng relative to the two other strains agreed with the observed decrease of flux towards CIT (Fig. 5a). The build-up of AKG in the PSP strain provided further evidence that the cMCS design directed more carbon towards the indigoidine precursors (Fig. 5a and Fig. S9). Overall, the increase of TCA cycle metabolites suggested TCA cycle flux congestion in the PSP strain (Fig. 4). Meanwhile, the decrease of intracellular CIT, AKG, and MAL in the Eng strain may be due to drainage of TCA cycle metabolites to produce indigoidine (requires two molecules of glutamine, derived from alpha-ketoglutarate, AKG). During the production phase (Fig. 5b), there was an overall reduction of intracellular metabolites after glucose depletion and most metabolite levels were similar between strains. However, there was a 1.7–fold increase in the AKG pool size in the PSP strain relative to the Eng strain, while 3–fold increase of intracellular SUC in the PSP strain was observed (Fig. S9).

3.4. Integration of omics data suggests new engineering strategies

The integrative analysis of the PSP strain was used to guide the next round of strain design to improve the bioconversion of glucose to indigoidine. The metabolite analyses indicated that there were the relatively small changes in the PSP flux network and limited growth phase production (in shaking flasks) and led to the question of whether the PSP strain production could be further improved if the CRISPRi repression was more complete in its knockdown efficacy. A random mutagenesis screen of the ribosome binding site (RBS) driving *cpf1* was performed to identify variants that resulted in higher expression levels (**Materials and Methods 2.9**). It is well established that introducing a CRISPR system targeting a chromosomal locus for cutting leads to cell death (Bikard et al., 2012). This phenotype was used to identify RBS variants for *F. novicida cpf1* expression where the concurrent introduction of a gRNA targeting *pyrF*/PP_1815 led to low CFUs in a WT strain but had no change on CFU counts in a Δ*pyrF* strain. The original RBS sequence for *cpf1* expression led to >500 CFU per μg plasmid DNA when transformed with the system targeting the *pyrF* locus. After screening ~50 RBS mutants, one candidate RBS was identified with the better cell-killing activity (~0–5 CFUs/μg plasmid DNA), implying it had improved function. The identified RBS sequence was then incorporated into the CRISPRi plasmid for glucose/indigoidine growth coupling to enhance expression

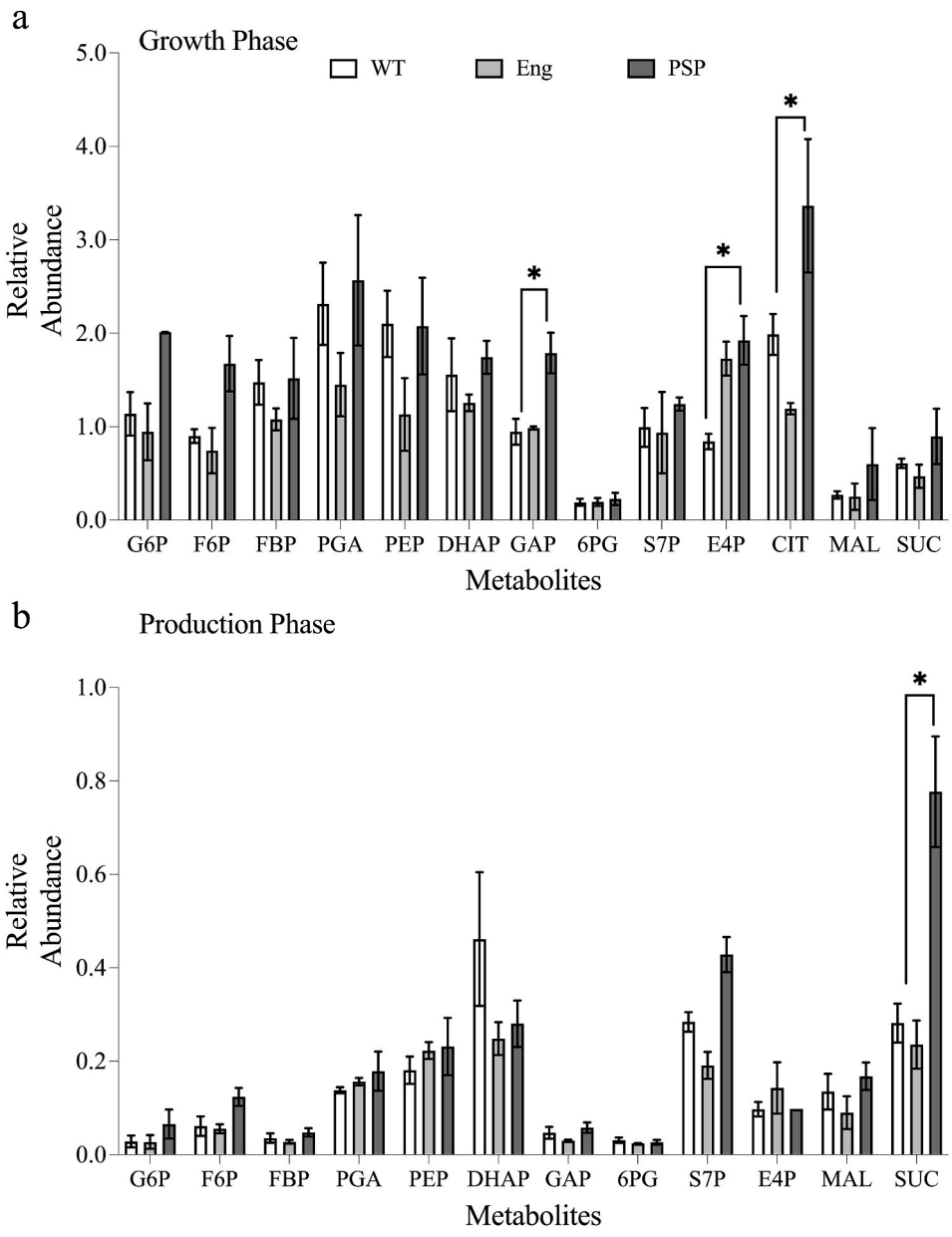

Fig. 5. Metabolite pool sizes. Comparison of metabolite pool sizes in the growth (a) and production (b) phases. Pool sizes were compared to a isotopically labeled internal standard (see **Methods Section**) with a relative abundance of one being equal pool sizes between the standard and strains) * denotes metabolite pool sizes that were significantly different between strains (p-value <0.05, one-way anova). **Citrate in panel (b) is reported as ng/mg of Dry cell weight (divided by 100 for visualization purposes). Error bars represent the standard error (n = 3), except for E4P in the PSP strain during production phase (n = 1). For metabolite abbreviations, refer to the list of abbreviations within the Supplementary Information.

(pTE442, Table 1). The reinforcement of the original cMCS design resulted in stronger growth coupling, with 1.6–fold (p-value = 0.08) improvement in production rate at the end of the growth-phase (6 h timepoint) compared to the PSP strain (Fig. 6). However, the increased production rate was not sustained over the course of cultivation and the strain only resulted in a 1.2–fold increase of titer (p-value = 0.14) at the final time point (72 h). The slowdown in production may have been due to the nitrogen limited regime near the end of the growth phase, despite the indication that the CRISPRi construct continued to affect pathway protein levels for at least 120 h (Banerjee et al., 2020).

After increasing the RBS strength, the omics data analysis identified four targets for further engineering. The first two came from observations of flux changes: 1. that the glyoxylate shunt was activated and allowed carbon to bypass the central carbon metabolism indigoidine precursor, AKG and, 2. that downregulation of the malate dehydrogenase reaction was not sufficient despite targeting three out of four enzymes involved in the reaction by CRISPRi (*mdh, mqo-II, mqo-II*, Fig. 4). Thus, two genes, isocitrate lyase, *aceA* (PP_4116) and the final malate dehydrogenase, *mqo-III* (PP_0751) were selected as deletion targets. The intracellular and extracellular metabolomic data sets demonstrated a build-up and secretion of succinate from the PSP strain (Figs. 3c and 5b) under the specific growth conditions tested. Reutilization of the accumulated succinate would not increase indigoidine production and thus represented a loss of carbon from the system (Fig. 3d and Fig. S6). The *sucC* (PP_4185) and *sucD* (PP_4186) subunits of succinyl-CoA synthetase complex were selected as the next gene targets to prevent succinate build-up and secretion. Similarly, the extracellular data indicated that knockdown of the gluconate forming glucose dehydrogenase (ΔPP_1444) was insufficient to fully prevent secretion of gluconate or 2 KG. PP_1444 was therefore selected for deletion to further shift production towards the growth phase. Finally, the *phaAZC-IID* operon responsible for synthesis of the storage compound polyhydroxyalkanoate (PHA) was selected for complete deletion. The PHA genes consistently appeared as deletion candidates in the cMCS design (Banerjee et al., 2020). The two genes targeted for downregulation (PP_5003 and PP_5005) by the CRISPRi construct catalyze the polymerization of PHA. While the two targeted PHA genes (PP_5003 and PP_5005) were down-regulated, several other genes involved in

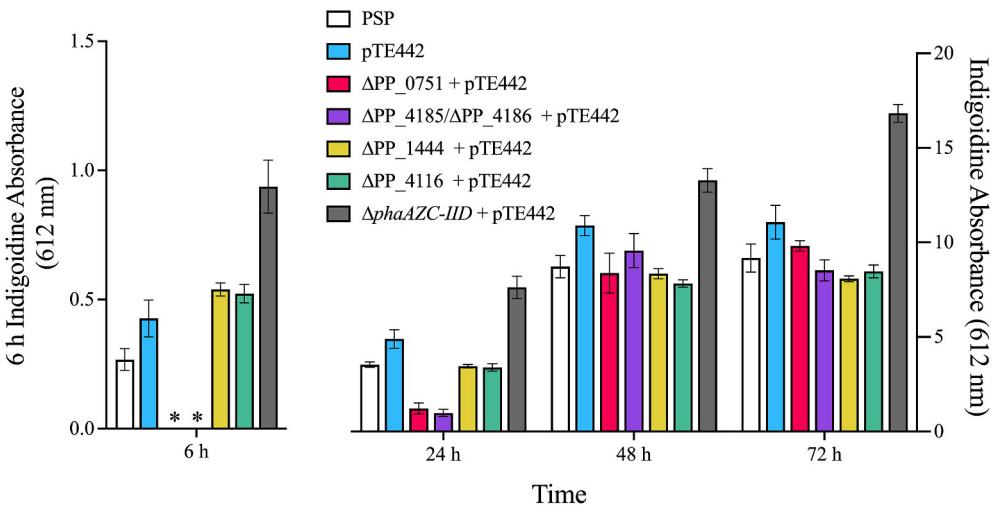

Fig. 6. Production profiling of various indigoidine producing strains. Indigoidine titers as measured by absorbance in DMSO at 612 nm. Strain pTE442 represents the indigoidine production strain containing plasmid pTE442 (Table 1). * denotes data points that were not collected due to no observable growth (see Fig. S10). The 6 h measurements are depicted on a separate axis due to differences in the scale of the measurements. The indigoidine absorbance for the Δ*phaAZC-IID* strain corresponds to ~0.2 ± 0.1 g/L at 6 h and ~3.6 ± 0.2 g/L at 72 h as determined with a previously reported standard curve (**see Methods Section 2.7** (Banerjee et al., 2020)). All measurements were from cultures grown in 14 mL volume in 50 mL shaking flasks and production medium (10 g/L glucose, 2 g/L $(NH_4)_2SO_4$, 3 g/L arabinose, 0.5 mM IPTG at time of induction. The PSP strain growth medium also contained 50 μg/L of kanamycin). Error bars represent standard error (n ≥ 6).

β-oxidation (forming precursors for PHA biosynthesis) were up-regulated compared to the Eng strain ((Banerjee et al., 2020), Table S3). PHA accession and biosynthetic gene clusters have been shown to be robust (Ankenbauer et al., 2020) in *P. putida* and to continue under nitrogen limited conditions. Thus, sufficient PHA flux may still occur and redirect carbon flux away from the indigoidine production route.

Next, each of the deletion strains (ΔPP_0751, ΔPP_1444, ΔPP_4116, ΔPP_4185ΔPP_4186, Δ*phaAZC-IID*) were constructed via ssDNA recombineering (see **Materials and Methods Section 2.10**) and tested for growth-coupled indigoidine production with the RBS-optimized CRISPRi plasmid (pTE442). Deletion of the PHA operon led to a significant (p-value < 0.01) increase in both production rate and titer across the cultivation (Fig. 6). The Δ*phaAZC-IID* strain had a 2.2–fold increase in production at the end of the growth phase compared to pTE442 strain, which was maintained throughout the cultivation and resulted in a 1.5–fold improvement of indigoidine titer at 72 h (p-values<0.01).

In contrast, deletion of *mqo-III* (ΔPP_0751) or the succinyl-CoA synthetase subunits (ΔPP_4185 ΔPP_4186) led to strains with substantial growth defects (reaching OD_{600} ~1–3 at 24 h) (Fig. S10). RB-TnSeq analysis previously indicated that no transposon mutants had been recovered in either of these gene loci, which provides indirect evidence that the genes may be essential (Eng et al., 2021; Price et al., 2018; Thompson et al., 2019). However, colonies were obtained for each deletion, although the strains exhibited a severe growth defect in liquid minimal medium. The deletion strains' fitness defects agreed with the previous RB-TnSeq results, and the first DBTL cycle workflow aimed at avoiding potentially essential metabolic reactions targets for CRISPRi knockdown. Of the remaining deletion strains, isocitrate dehydrogenase (ΔPP_4116) or glucose dehydrogenase (ΔPP_1444) led to a 1.2– and 1.3–fold increase in production for the respective strains at the end of the growth phase over the strain containing the improved RBS (pTE442), albeit the increase was not significant (p-values = 0.21 and 0.17, respectively) (Fig. 6). The production rates slowed over the course of cultivation and the deletions were detrimental to overall titers with 1.3– and 1.4– fold decreases compared to the pTE442 strain observed at 72 h (p-values <0.05). Both the ΔPP_4116 and ΔPP_1444 strains also had decreased production compared to the original PSP strain by the end of the cultivation (by 8% (p-value >0.05) and 10% (p-value <0.05), respectively). Overall, these results indicated that the modified RBS used to drive *cpf1* expression increased production 60% during the exponential phase compared to the original PSP design while further deletion of the *pha* operon led to a 220% increase over the PSP design. Moreover, final product titer improvements could be detected concomitant with growth in exponential phase, in stationary phase, or both.

4. Discussion

4.1. *P. putida* metabolic plasticity and flux buffering

Cellular metabolism has evolved over time to provide robust flux networks for generating the precursors and energy molecules necessary for growth and survival under a variety of environmental and genetic perturbations (Czajka et al., 2020b; Donati et al., 2021). Changes in protein levels can be counteracted by latent pathway activation, enzyme activity changes (through post-transcriptional regulation), or metabolite levels changes (Raamsdonk et al., 2001; Wegner et al., 2015). The resulting flux buffering determines the effectiveness of CRISPRi modifications and requires integrated flux and metabolite analyses. Studies have shown that multiplexed CRISPRi strategies can overcome the flux buffering and reroute carbon in a manner that increases product production (Banerjee et al., 2020; Reis et al., 2019; Tian et al., 2019), but whether the CRISPRi-mediated gene repression led to decreased flux had not been directly investigated. In the PSP strain, targeting 14 genes for downregulation indirectly led to the downregulation of 167 genes and the upregulation of 139 genes compared to the Eng control strain carrying an empty vector plasmid, pTE219 (Table 1, Fig. 1, Fig. S4). The transcriptomics analysis was unable to detect the subtle flux changes characterized by the fluxomics analysis or the near-complete inactivation of *maeB*/PP_5085 in the PSP strain (Fig. 4), likely due to post-translational regulatory mechanisms that cannot be captured at the RNA enrichment level or high basal mRNA degradation rates that blunt this assay's sensitivity in prokaryotes (Herzel et al., 2022).

The ^{13}C-MFA revealed several enzymatic rates were undesirable based on the original cMCS design and potential deletion targets for further strain improvement (Fig. 4, Supplemental DataFile 2). Specifically, there was an increase of flux through the malate dehydrogenase reaction despite targeted downregulation of three out of four of the genes involved in this step. It appeared that limiting flux through the malic enzyme resulted in flux rerouting through the malate dehydrogenase reaction and further perturbations downstream, indicating that the malic enzyme and the pyruvate shunt are key nodes with limited flux buffering for *P. putida* to maintain stable flux through the TCA cycle. These observations are supported by studies that showed the malic

enzyme/malate dehydrogenase flux ratio shifts in response to oxidative stress (Nikel et al., 2021) or iron limitations (Sasnow et al., 2016) from its normal ratio of ~65% TCA cycle flux entering the pyruvate shunt (Kohlstedt and Wittmann, 2019; Nikel et al., 2015, 2021). A recent study analyzing kinetic parameters and control coefficients in *P. putida* indicated that the malic enzyme exhibits control over the pyruvate shunt and has increased importance under stress conditions (Tokic et al., 2020). Thus, *P. putida* appears to employ highly active anaplerotic pathways to maintain relatively stable fluxes through the core pathways.

The original cMCS design called for complete gene deletions and predicted decreased flux through the second half of the TCA cycle (SUC → MAL) compared to the experimental ^{13}C-MFA measured activity ((Banerjee et al., 2020), **Supplementary DataFile 2**). Deletion strains generated to reduce the malate dehydrogenase activity (ΔPP_0751) and the glyoxylate shunt flux (ΔPP_4116) to match the cMCS original design resulted in a severe growth defect and reduced production at 72 h (by 13% and 30%, respectively (Fig. 6)). Logically extending the deletion results obtained here, it follows that implementing the original cMCS design as a 14-gene deletion strain would have generated a strain with significantly slower growth and lower production overall compared to the multiplexed CRISPRi implementation. Integrating gene essentiality indicators into computational designs can help avoid the generation of growth-defected strains. As gene essentiality information may not be available or complete, multiplexed CRISPRi constructs offer an alternative implementation that can avoid gene essentiality issues by allowing for minimal flux through such nodes while still leading to desired phenotypes. To illustrate this, consider the indigoidine production titer when PP_4116 expression was reduced versus its complete deletion; according to RNAseq and proteomics, CRISPRi knockdown reduced PP_4116 levels by ~30% (Table S3). In contrast, when PP_4116 is completely abolished in the case of a gene deletion, the impact on indigoidine titer was not beneficial overall and even led to an 8% decreased production compared to the original PSP strain at 120 h. While gene deletions lead to desirable re-routing fluxes in cases of simple pathways (i.e., one to two deletions), it eliminates pathways needed for the metabolic networks to accommodate further stresses. For complex engineering designs calling for multiple deletions, the resulting flux network may be too constrained and unable to maintain flexibility to compensate for both production burdens and modulation of pathways by engineered tools (Chavarría et al., 2012). Thus, utilizing CRISPRi to modulate cellular fluxes allows cells to maintain the necessary flux network flexibility that can result in stable growth and robust production in cases of complex strain designs. However, it was determined that CRISPRi mediated downregulation would not impose flux changes predicted to be necessary from cMCS modeling tools. These CRISPRi implementations may provide an accessible route to prototype large gene cutsets before laboriously building sequential gene deletion strains to realize the predicted gains in titers, rates, and yields.

4.2. Engineering insights on growth coupling and cellular byproducts

Growth coupling has been demonstrated as a viable strategy for improving production of non-toxic compounds like indigoidine, itaconic acid, and 1,4-butanediol (Banerjee et al., 2020; Harder et al., 2016; Yim et al., 2011). The generated PSP strain indicated large gene cut sets could be rapidly tested using multiplex CRISPRi/dCpf1, but did not result in complete gene inactivation (Banerjee et al., 2020). Accordingly, in this study it was shown that increased CRISPRi activity was realized with an optimal Cpf1-RBS sequence and revealed higher indigoidine production titers in the growth phase where 60% more product was detected at the 6 h timepoint.

Several specific gene targets from the CRISPR multiplex set were re-evaluated to determine if partial knockdown of a single metabolic reaction could explain the predicted titers, rates, and yields were not reached. Of the deletion strains tested in tandem with the CRISPRi system, inactivating PHA synthesis was the most effective strategy and led to a 2.2–fold improvement in growth phase production and 1.5–fold more indigoidine at the end of cultivation compared to the pTE442 strain (Fig. 6). PHAs are typically synthesized as storage compounds that are accessed under glucose starvation (Ankenbauer et al., 2020) in *P. putida* and have been previously shown to be closely tied to central carbon metabolism (de Eugenio et al., 2010a, 2010b; Escapa et al., 2012). Preventing PHA formation in *P. putida* may be beneficial for indigoidine production because blocking synthesis increases acetyl-CoA and precursor flux through the TCA cycle (Escapa et al., 2012) and has also been predicted to increase ATP production (Manoli et al., 2022). Furthermore, PHA synthesis has been identified as a key component in maintaining energy and redox balance by allowing for dissipation of excess energy (Manoli et al., 2022). Disrupting this energy balancing component may further drive the production of indigoidine as a means to dissipate reducing power. Overall, the *phaAZC-IID* deletions generated here prevented the accumulation of this key carbon storage component and enabled the strain to redirect excess carbon and energy to production of indigoidine throughout the cultivation process.

Under the studied production conditions in M9 minimal media, the pTE442 strain was nitrogen limited. As this strain provides an example of growth coupled product production, extending the growth phase and relieving the nitrogen limitation through increased initial indigoidine or a with a nitrogen supplemented feed during cultivation is expected to result in further production improvements between strains as shown in previous work (Banerjee et al., 2020; Wehrs et al., 2019). This strategy could enhance the effectiveness of the CRISPRi construct as well since many of the CRISPRi gene targets are involved in central carbon metabolism and amino acid synthesis pathways that become less active as glucose is depleted.

5. Conclusions

Initial DBTL cycles can be effective in increasing production from engineered strains, but systems analyses are necessary to reveal cell metabolic regulations and to identify non-intuitive engineering targets in advanced cycles (Zhang et al., 2020). Here, multi-omics data provided holistic information on the *P. putida* system-wide response to complex metabolic perturbations that helped re-engineer a strain for a nearly 50% improvement in heterologous production titer over the first round engineered strain. Although multi-omic analyses can lead to understanding of metabolic status and regulations in light of genetic modifications and cultivation stresses, the obtained metabolic knowledge may not directly pinpoint new gene targets after initial DBTL rounds. Integrating multi-omic data into genome-scale models (Kim and Lun, 2014; Martín et al., 2015; Töpfer et al., 2015), utilizing computational design algorithms (Klamt and Mahadevan, 2015), and high throughput strain construction and evaluation can result in more robust and accurate genetic targets for DBTL applications.

Author contributions

JC DB TE YT and AM conceived the study. CY JM TE constructed and verified recombinant *P. putida* strains and plasmids. JC harvested and analyzed samples for ^{13}C MFA analysis. NMM, BCP and YMK acquired and analyzed samples for the MFA analysis of metabolites and proteogenic amino acids using high resolution mass spectrometry. JC DB TE YT and AM interpreted the results. JC wrote the first draft of the manuscript and prepared figures. All authors edited and provided constructive feedback on the final manuscript. All authors have read and approved the final version of this manuscript for publication.

Data availability

The sequences of the plasmids generated in this study may be visualized at public-registry.jbei.org. All other data is included in the manuscript and the supplementary files. The INCA network models have

been provided as matlab files with the conditions used to simulate the flux network results.

Declaration of competing interest

The authors declare no conflicts of interest.

Acknowledgements

We thank Victor de Lorenzo and Esteban Martínez (Centro Nacional de Biotecnología-CSIC) for insightful technical comments and sharing their recombineering plasmids and methods. We thank Patrick Leggieri & Michelle O'Malley (University of California, Santa Barbara) as well as Chris Lawson (University of Toronto) for insightful comments and suggestions on the manuscript. JC was supported by the U.S. Department of Energy, Office of Science, Office of Workforce Development for Teachers and Scientists, Office of Science Graduate Student Research (SCGSR) program. The SCGSR program is administered by the Oak Ridge Institute for Science and Education (ORISE) for the DOE. ORISE is managed by Oak Ridge Associated Universities (ORAU) under contract number DE-SC001464. All opinions expressed in this paper are the author's and do not necessarily reflect the policies and views of ODE, ORAU, or ORISE.

A part of this research was conducted at the Joint BioEnergy Institute (http://www.jbei.org) supported by the US Department of Energy, Office of Science, through contract DE-AC02-05CH11231 between Lawrence Berkeley National Laboratory (LBNL) and the US Department of Energy. Separately, a portion of this research was performed on a project award 10.46936/brcr.proj.2021.51792/60000322 from the Environmental Molecular Sciences Laboratory (EMSL), a DOE Office of Science User Facility sponsored by the Biological and Environmental Research program under Contract No. DE-AC05-76RL01830 at Pacific Northwest National Laboratory (PNNL). The work was partially supported by Agile BioFoundry (http://agilebiofoundry.org), funded by the United States Department of Energy, Office of Energy Efficiency and Renewable Energy, Bioenergy Technologies Office, under Award No. DE-NL0030038. The funders had no role in study design, data collection and analysis, decision to publish, or preparation of the manuscript.

We also acknowledge the Proteomics and Mass Spectrometry Core Facility at the Donald Danforth Plant Science Center and the United States Department of Agriculture, Agricultural Research Service, for access and use of instrumentation and resources. In addition, we acknowledge support from the National Science Foundation (NSF-MCB #1616820 and NSF-DBI #1427621), the latter grant provided support for acquisition of the QTRAP LC-MS/MS used for collecting initial data in this project.

Appendix A. Supplementary data

Supplementary data to this article can be found online at https://doi.org/10.1016/j.mec.2022.e00206.

References

Abernathy, M.H., Yu, J., Ma, F., Liberton, M., Ungerer, J., Hollinshead, W.D., Gopalakrishnan, S., He, L., Maranas, C.D., Pakrasi, H.B., Allen, D.K., Tang, Y.J., 2017. Deciphering cyanobacterial phenotypes for fast photoautotrophic growth via isotopically nonstationary metabolic flux analysis. Biotechnol. Biofuels 10, 273. https://doi.org/10.1186/s13068-017-0958-y.

Ankenbauer, A., Schäfer, R.A., Viegas, S.C., Pobre, V., Voß, B., Arraiano, C.M., Takors, R., 2020. Pseudomonas putida KT2440 is naturally endowed to withstand industrial-scale stress conditions. Microb. Biotechnol. 13, 1145–1161. https://doi.org/10.1111/1751-7915.13571.

Aparicio, T., Nyerges, A., Martínez-García, E., de Lorenzo, V., 2020. High-efficiency multi-site genomic editing of Pseudomonas putida through thermoinducible ssDNA recombineering. iScience 23, 100946. https://doi.org/10.1016/j.isci.2020.100946.

Arnold, S., Henkel, M., Wanger, J., Wittgens, A., Rosenau, F., Hausmann, R., 2019. Heterologous rhamnolipid biosynthesis by P. putida KT2440 on bio-oil derived small organic acids and fractions. Amb. Express 9, 80. https://doi.org/10.1186/s13568-019-0804-7.

Askitosari, T.D., Boto, S.T., Blank, L.M., Rosenbaum, M.A., 2019. Boosting heterologous phenazine production in Pseudomonas putida KT2440 through the exploration of the natural sequence space. Front. Microbiol. 10, 1990. https://doi.org/10.3389/fmicb.2019.01990.

Banerjee, D., Eng, T., Lau, A.K., Sasaki, Y., Wang, B., Chen, Y., Prahl, J.-P., Singan, V.R., Herbert, R.A., Liu, Y., Tanjore, D., Petzold, C.J., Keasling, J.D., Mukhopadhyay, A., 2020. Genome-scale metabolic rewiring improves titers rates and yields of the non-native product indigoidine at scale. Nat. Commun. 11, 5385. https://doi.org/10.1038/s41467-020-19171-4.

Beckers, V., Poblete-Castro, I., Tomasch, J., Wittmann, C., 2016. Integrated analysis of gene expression and metabolic fluxes in PHA-producing Pseudomonas putida grown on glycerol. Microb. Cell Factories 15, 73. https://doi.org/10.1186/s12934-016-0470-2.

Bikard, D., Hatoum-Aslan, A., Mucida, D., Marraffini, L.A., 2012. CRISPR interference can prevent natural transformation and virulence acquisition during in vivo bacterial infection. Cell Host Microbe 12, 177–186. https://doi.org/10.1016/j.chom.2012.06.003.

Chavarría, M., Kleijn, R.J., Sauer, U., Pflüger-Grau, K., de Lorenzo, V., 2012. Regulatory tasks of the phosphoenolpyruvate-phosphotransferase system of Pseudomonas putida in central carbon metabolism. mBio 3. https://doi.org/10.1128/mBio.00028-12.

Czajka, J.J., Kambhampati, S., Tang, Y.J., Wang, Y., Allen, D.K., 2020a. Application of stable isotope tracing to elucidate metabolic dynamics during yarrowia lipolytica α-ionone fermentation. iScience 23, 100854. https://doi.org/10.1016/j.isci.2020.100854.

Czajka, J.J., Okumuş, B., Koffas, M.A., Blenner, M., Tang, Y.J., 2020b. Mitigation of host cell mutations and regime shift during microbial fermentation: a perspective from flux memory. Curr. Opin. Biotechnol. 66, 227–235. https://doi.org/10.1016/j.copbio.2020.08.003.

Dagley, M.J., McConville, M.J., 2018. DExSI: a new tool for the rapid quantitation of 13C-labelled metabolites detected by GC-MS. Bioinformatics 34, 1957–1958. https://doi.org/10.1093/bioinformatics/bty025.

de Eugenio, L.I., Escapa, I.F., Morales, V., Dinjaski, N., Galán, B., García, J.L., Prieto, M.A., 2010a. The turnover of medium-chain-length polyhydroxyalkanoates in Pseudomonas putida KT2442 and the fundamental role of PhaZ depolymerase for the metabolic balance. Environ. Microbiol. 12, 207–221. https://doi.org/10.1111/j.1462-2920.2009.02061.x.

de Eugenio, L.I., Galán, B., Escapa, I.F., Maestro, B., Sanz, J.M., García, J.L., Prieto, M.A., 2010b. The PhaD regulator controls the simultaneous expression of the pha genes involved in polyhydroxyalkanoate metabolism and turnover in Pseudomonas putida KT2442. Environ. Microbiol. 12, 1591–1603. https://doi.org/10.1111/j.1462-2920.2010.02199.x.

del Castillo, T., Ramos, J.L., Rodríguez-Herva, J.J., Fuhrer, T., Sauer, U., Duque, E., 2007. Convergent peripheral pathways catalyze initial glucose catabolism in Pseudomonas putida: genomic and flux analysis. J. Bacteriol. 189, 5142–5152. https://doi.org/10.1128/JB.00203-07.

Deng, W.P., Nickoloff, J.A., 1992. Site-directed mutagenesis of virtually any plasmid by eliminating a unique site. Anal. Biochem. 200, 81–88. https://doi.org/10.1016/0003-2697(92)90280-K.

Donati, S., Kuntz, M., Pahl, V., Farke, N., Beuter, D., Glatter, T., Gomes-Filho, J.V., Randau, L., Wang, C.-Y., Link, H., 2021. Multi-omics analysis of CRISPRi-knockdowns identifies mechanisms that buffer decreases of enzymes in E. coli metabolism. Cell Syst 12, 56–67. https://doi.org/10.1016/j.cels.2020.10.011 e6.

Dong, J., Chen, Y., Benites, V.T., Baidoo, E.E.K., Petzold, C.J., Beller, H.R., Eudes, A., Scheller, H.V., Adams, P.D., Mukhopadhyay, A., Simmons, B.A., Singer, S.W., 2019. Methyl ketone production by Pseudomonas putida is enhanced by plant-derived amino acids. Biotechnol. Bioeng. 116, 1909–1922. https://doi.org/10.1002/bit.26995.

Eng, T., Banerjee, D., Lau, A.K., Bowden, E., Herbert, R.A., Trinh, J., Prahl, J.-P., Deutschbauer, A., Tanjore, D., Mukhopadhyay, A., 2021. Engineering Pseudomonas putida for efficient aromatic conversion to bioproduct using high throughput screening in a bioreactor. Metab. Eng. 66, 229–238. https://doi.org/10.1016/j.ymben.2021.04.015.

Escapa, I.F., García, J.L., Bühler, B., Blank, L.M., Prieto, M.A., 2012. The polyhydroxyalkanoate metabolism controls carbon and energy spillage in Pseudomonas putida. Environ. Microbiol. 14, 1049–1063. https://doi.org/10.1111/j.1462-2920.2011.02684.x.

Harder, B.-J., Bettenbrock, K., Klamt, S., 2016. Model-based metabolic engineering enables high yield itaconic acid production by Escherichia coli. Metab. Eng. 38, 29–37. https://doi.org/10.1016/j.ymben.2016.05.008.

Herzel, L., Stanley, J.A., Yao, C.-C., Li, G.-W., 2022. Ubiquitous mRNA decay fragments in E. coli redefine the functional transcriptome. Nucleic Acids Res. 50, 5029–5046. https://doi.org/10.1093/nar/gkac295.

He, L., Wu, S.G., Zhang, M., Chen, Y., Tang, Y.J., 2016. WUFlux: an open-source platform for 13C metabolic flux analysis of bacterial metabolism. BMC Bioinf. 17, 444. https://doi.org/10.1186/s12859-016-1314-0.

He, L., Xiao, Y., Gebreselassie, N., Zhang, F., Antoniewiez, M.R., Tang, Y.J., Peng, L., 2014. Central metabolic responses to the overproduction of fatty acids in Escherichia coli based on 13C-metabolic flux analysis. Biotechnol. Bioeng. 111, 575–585. https://doi.org/10.1002/bit.25124.

He, P., Wan, N., Cai, D., Hu, S., Chen, Y., Li, S., Chen, S., 2019. 13C-Metabolic flux analysis reveals the metabolic flux redistribution for enhanced production of poly-γ-glutamic acid in dlt over-expressed Bacillus licheniformis. Front. Microbiol. 10, 105. https://doi.org/10.3389/fmicb.2019.00105.

Hollinshead, W., He, L., Tang, Y.J., 2019. 13C-Fingerprinting and metabolic flux analysis of bacterial metabolisms. Methods Mol. Biol. 1927, 215–230. https://doi.org/10.1007/978-1-4939-9142-6_15.

Kim, M.K., Lun, D.S., 2014. Methods for integration of transcriptomic data in genome-scale metabolic models. Comput. Struct. Biotechnol. J. 11, 59–65. https://doi.org/10.1016/j.csbj.2014.08.009.

Klamt, S., Mahadevan, R., 2015. On the feasibility of growth-coupled product synthesis in microbial strains. Metab. Eng. 30, 166–178. https://doi.org/10.1016/j.ymben.2015.05.006.

Kohlstedt, M., Wittmann, C., 2019. GC-MS-based 13C metabolic flux analysis resolves the parallel and cyclic glucose metabolism of Pseudomonas putida KT2440 and Pseudomonas aeruginosa PAO1. Metab. Eng. 54, 35–53. https://doi.org/10.1016/j.ymben.2019.01.008.

Long, C.P., Antoniewicz, M.R., 2019a. High-resolution 13C metabolic flux analysis. Nat. Protoc. 14, 2856–2877. https://doi.org/10.1038/s41596-019-0204-0.

Long, C.P., Antoniewicz, M.R., 2019b. Metabolic flux responses to deletion of 20 core enzymes reveal flexibility and limits of E. coli metabolism. Metab. Eng. 55, 249–257. https://doi.org/10.1016/j.ymben.2019.08.003.

Long, C.P., Gonzalez, J.E., Sandoval, N.R., Antoniewicz, M.R., 2016. Characterization of physiological responses to 22 gene knockouts in Escherichia coli central carbon metabolism. Metab. Eng. 37, 102–113. https://doi.org/10.1016/j.ymben.2016.05.006.

Manoli, M.-T., Nogales, J., Prieto, A., 2022. Synthetic control of metabolic states in Pseudomonas putida by tuning polyhydroxyalkanoate cycle. mBio, e0179421. https://doi.org/10.1128/mbio.01794-21.

Martín, H.G., Kumar, V.S., Weaver, D., Ghosh, A., Chubukov, V., Mukhopadhyay, A., Arkin, A., Keasling, J.D., 2015. A method to constrain genome-scale models with 13C labeling data. PLoS Comput. Biol. 11, e1004363 https://doi.org/10.1371/journal.pcbi.1004363.

Molina, L., La Rosa, R., Nogales, J., Rojo, F., 2019a. Influence of the Crc global regulator on substrate uptake rates and the distribution of metabolic fluxes in Pseudomonas putida KT2440 growing in a complete medium. Environ. Microbiol. 21, 4446–4459. https://doi.org/10.1111/1462-2920.14812.

Molina, L., Rosa, R.L., Nogales, J., Rojo, F., 2019b. Pseudomonas putida KT2440 metabolism undergoes sequential modifications during exponential growth in a complete medium as compounds are gradually consumed. Environ. Microbiol. 21, 2375–2390. https://doi.org/10.1111/1462-2920.14622.

Nakayasu, E.S., Nicora, C.D., Sims, A.C., Burnum-Johnson, K.E., Kim, Y.-M., Kyle, J.E., Matzke, M.M., Shukla, A.K., Chu, R.K., Schepmoes, A.A., Jacobs, J.M., Baric, R.S., Webb-Robertson, B.-J., Smith, R.D., Metz, T.O., 2016. MPLEx: a robust and universal protocol for single-sample integrative proteomic, metabolomic, and lipidomic analyses. mSystems 1. https://doi.org/10.1128/mSystems.00043-16.

Nieto, C., Fernández-Tresguerres, E., Sánchez, N., Vicente, M., Díaz, R., 1990. Cloning vectors, derived from a naturally occurring plasmid of Pseudomonas savastanoi, specifically tailored for genetic manipulations in Pseudomonas. Gene 87, 145–149. https://doi.org/10.1016/0378-1119(90)90507-N.

Nikel, P.I., Chavarría, M., Fuhrer, T., Sauer, U., de Lorenzo, V., 2015. *Pseudomonas putida* KT2440 strain metabolizes glucose through a cycle formed by enzymes of the entner-doudoroff, embden-meyerhof-parnas, and pentose phosphate pathways. J. Biol. Chem. 290, 25920–25932. https://doi.org/10.1074/jbc.M115.687749.

Nikel, P.I., de Lorenzo, V., 2018. *Pseudomonas putida* as a functional chassis for industrial biocatalysis: from native biochemistry to trans-metabolism. Metab. Eng. 50, 142–155. https://doi.org/10.1016/j.ymben.2018.05.005.

Nikel, P.I., Fuhrer, T., Chavarría, M., Sánchez-Pascuala, A., Sauer, U., de Lorenzo, V., 2021. Reconfiguration of metabolic fluxes in Pseudomonas putida as a response to sub-lethal oxidative stress. ISME J. 15, 1751–1766. https://doi.org/10.1038/s41396-020-00884-9.

Niu, W., Willett, H., Mueller, J., He, X., Kramer, L., Ma, B., Guo, J., 2020. Direct biosynthesis of adipic acid from lignin-derived aromatics using engineered Pseudomonas putida KT2440. Metab. Eng. 59, 151–161. https://doi.org/10.1016/j.ymben.2020.02.006.

Nogales, J., Mueller, J., Gudmundsson, S., Canalejo, F.J., Duque, E., Monk, J., Feist, A. M., Ramos, J.L., Niu, W., Palsson, B.O., 2020. High-quality genome-scale metabolic modelling of *Pseudomonas putida* highlights its broad metabolic capabilities. Environ. Microbiol. 22, 255–269. https://doi.org/10.1111/1462-2920.14843.

Pedersen, B.H., Gurdo, N., Johansen, H.K., Molin, S., Nikel, P.I., La Rosa, R., 2021. High-throughput dilution-based growth method enables time-resolved exo-metabolomics of Pseudomonas putida and Pseudomonas aeruginosa. Microb. Biotechnol. 14, 2214–2226. https://doi.org/10.1111/1751-7915.13905.

Pomraning, K.R., Dai, Z., Munoz, N., Kim, Y.-M., Gao, Y., Deng, S., Kim, J., Hofstad, B.A., Swita, M.S., Lemmon, T., Collett, J.R., Panisko, E.A., Webb-Robertson, B.-J.M., Zucker, J.D., Nicora, C.D., De Paoli, H., Baker, S.E., Burnum-Johnson, K.E., Hillson, N.J., Magnuson, J.K., 2021. Integration of proteomics and metabolomics into the design, build, test, learn cycle to improve 3-hydroxypropionic acid production in Aspergillus pseudoterreus. Front. Bioeng. Biotechnol. 9, 603832 https://doi.org/10.3389/fbioe.2021.603832.

Price, M.N., Wetmore, K.M., Waters, R.J., Callaghan, M., Ray, J., Liu, H., Kuehl, J.V., Melnyk, R.A., Lamson, J.S., Suh, Y., Carlson, H.K., Esquivel, Z., Sadeeshkumar, H., Chakraborty, R., Zane, G.M., Rubin, B.E., Wall, J.D., Visel, A., Bristow, J., Blow, M. J., Deutschbauer, A.M., 2018. Mutant phenotypes for thousands of bacterial genes of unknown function. Nature 557, 503–509. https://doi.org/10.1038/s41586-018-0124-0.

Raamsdonk, L.M., Teusink, B., Broadhurst, D., Zhang, N., Hayes, A., Walsh, M.C., Berden, J.A., Brindle, K.M., Kell, D.B., Rowland, J.J., Westerhoff, H.V., van Dam, K., Oliver, S.G., 2001. A functional genomics strategy that uses metabolome data to reveal the phenotype of silent mutations. Nat. Biotechnol. 19, 45–50. https://doi.org/10.1038/83496.

Reis, A.C., Halper, S.M., Vezeau, G.E., Cetnar, D.P., Hossain, A., Clauer, P.R., Salis, H.M., 2019. Simultaneous repression of multiple bacterial genes using nonrepetitive extra-long sgRNA arrays. Nat. Biotechnol. 37, 1294–1301. https://doi.org/10.1038/s41587-019-0286-9.

Salis, H.M., Mirsky, E.A., Voigt, C.A., 2009. Automated design of synthetic ribosome binding sites to control protein expression. Nat. Biotechnol. 27, 946–950. https://doi.org/10.1038/nbt.1568.

Sasnow, S.S., Wei, H., Aristilde, L., 2016. Bypasses in intracellular glucose metabolism in iron-limited *Pseudomonas putida*. Microbiol. 5, 3–20. https://doi.org/10.1002/mbo3.287.

Silvis, M.R., Rajendram, M., Shi, H., Osadnik, H., Gray, A.N., Cesar, S., Peters, J.M., Hearne, C.C., Kumar, P., Todor, H., Huang, K.C., Gross, C.A., 2021. Morphological and transcriptional responses to CRISPRi knockdown of essential genes in Escherichia coli. mBio 12, e0256121. https://doi.org/10.1128/mBio.02561-21.

Thompson, M.G., Blake-Hedges, J.M., Cruz-Morales, P., Barajas, J.F., Curran, S.C., Eiben, C.B., Harris, N.C., Benites, V.T., Gin, J.W., Sharpless, W.A., Twigg, F.F., Skyrud, W., Krishna, R.N., Pereira, J.H., Baidoo, E.E.K., Petzold, C.J., Adams, P.D., Arkin, A.P., Deutschbauer, A.M., Keasling, J.D., 2019. Massively parallel fitness profiling reveals multiple novel enzymes in Pseudomonas putida lysine metabolism. mBio 10. https://doi.org/10.1128/mBio.02577-18.

Tian, T., Kang, J.W., Kang, A., Lee, T.S., 2019. Redirecting metabolic flux via combinatorial multiplex CRISPRi-mediated repression for isopentenol production in Escherichia coli. ACS Synth. Biol. 8, 391–402. https://doi.org/10.1021/acssynbio.8b00429.

Tokic, M., Hatzimanikatis, V., Miskovic, L., 2020. Large-scale kinetic metabolic models of Pseudomonas putida KT2440 for consistent design of metabolic engineering strategies. Biotechnol. Biofuels 13, 33. https://doi.org/10.1186/s13068-020-1665-7.

Töpfer, N., Kleessen, S., Nikoloski, Z., 2015. Integration of metabolomics data into metabolic networks. Front. Plant Sci. 6, 49. https://doi.org/10.3389/fpls.2015.00049.

Trinh, C.T., Wlaschin, A., Srienc, F., 2009. Elementary mode analysis: a useful metabolic pathway analysis tool for characterizing cellular metabolism. Appl. Microbiol. Biotechnol. 81, 813–826. https://doi.org/10.1007/s00253-008-1770-1.

Wahl, S.A., Dauner, M., Wiechert, W., 2004. New tools for mass isotopomer data evaluation in (13)C flux analysis: mass isotope correction, data consistency checking, and precursor relationships. Biotechnol. Bioeng. 85, 259–268. https://doi.org/10.1002/bit.10909.

Wang, Q., Mueller, A.P., Leong, C.R., Matsumoto, K., Taguchi, S., Nomura, C.T., 2009. Quick and efficient method for genetic transformation of biopolymer-producing bacteria. J. Chem. Technol. Biotechnol. 85, 775–778. https://doi.org/10.1002/jctb.2284.

Wannier, T.M., Nyerges, A., Kuchwara, H.M., Czikkely, M., Balogh, D., Filsinger, G.T., Borders, N.C., Gregg, C.J., Lajoie, M.J., Rios, X., Pál, C., Church, G.M., 2020. Improved bacterial recombineering by parallelized protein discovery. Proc. Natl. Acad. Sci. U.S.A. 117, 13689–13698. https://doi.org/10.1073/pnas.2001588117.

Wegner, A., Meiser, J., Weindl, D., Hiller, K., 2015. How metabolites modulate metabolic flux. Curr. Opin. Biotechnol. 34, 16–22. https://doi.org/10.1016/j.copbio.2014.11.008.

Wehrs, M., Gladden, J.M., Liu, Y., Platz, L., Prahl, J.-P., Moon, J., Papa, G., Sundstrom, E., Geiselman, G.M., Tanjore, D., Keasling, J.D., Pray, T.R., Simmons, B. A., Mukhopadhyay, A., 2019. Sustainable bioproduction of the blue pigment indigoidine: expanding the range of heterologous products in *R. toruloides* to include non-ribosomal peptides. Green Chem. 21, 3394–3406. https://doi.org/10.1039/C9GC00920E.

Wiechert, W., Schweissgut, O., Takanaga, H., Frommer, W.B., 2007. Fluxomics: mass spectrometry versus quantitative imaging. Curr. Opin. Plant Biol. 10, 323–330. https://doi.org/10.1016/j.pbi.2007.04.015.

Xu, F., Ke, X., Hong, M., Huang, M., Chen, C., Tian, X., Hang, H., Chu, J., 2021. Exploring the metabolic fate of propanol in industrial erythromycin-producing strain via 13C labeling experiments and enhancement of erythromycin production by rational metabolic engineering of Saccharopolyspora erythraea. Biochem. Biophys. Res. Commun. 542, 73–79. https://doi.org/10.1016/j.bbrc.2021.01.024.

Yang, S., Li, S., Jia, X., 2019. Production of medium chain length polyhydroxyalkanoate from acetate by engineered Pseudomonas putida KT2440. J. Ind. Microbiol. Biotechnol. 46, 793–800. https://doi.org/10.1007/s10295-019-02159-5.

Yim, H., Haselbeck, R., Niu, W., Pujol-Baxley, C., Burgard, A., Boldt, J., Khandurina, J., Trawick, J.D., Osterhout, R.E., Stephen, R., Estadilla, J., Teisan, S., Schreyer, H.B., Andrae, S., Yang, T.H., Lee, S.Y., Burk, M.J., Van Dien, S., 2011. Metabolic engineering of Escherichia coli for direct production of 1,4-butanediol. Nat. Chem. Biol. 7, 445–452. https://doi.org/10.1038/nchembio.580.

Young, J.D., 2014. INCA: a computational platform for isotopically non-stationary metabolic flux analysis. Bioinformatics 30, 1333–1335. https://doi.org/10.1093/bioinformatics/btu015.

You, L., He, L., Tang, Y.J., 2015. Photoheterotrophic fluxome in Synechocystis sp. strain PCC 6803 and its implications for cyanobacterial bioenergetics. J. Bacteriol. 197, 943–950. https://doi.org/10.1128/JB.02149-14.

Zhang, J., Petersen, S.D., Radivojevic, T., Ramirez, A., Pérez-Manríquez, A., Abeliuk, E., Sánchez, B.J., Costello, Z., Chen, Y., Fero, M.J., Martin, H.G., Nielsen, J., Keasling, J. D., Jensen, M.K., 2020. Combining mechanistic and machine learning models for predictive engineering and optimization of tryptophan metabolism. Nat. Commun. 11, 4880. https://doi.org/10.1038/s41467-020-17910-1.

Zhao, R., Liu, Y., Zhang, H., Chai, C., Wang, J., Jiang, W., Gu, Y., 2019. CRISPR-Cas12a-Mediated gene deletion and regulation in Clostridium ljungdahlii and its application

in carbon flux redirection in synthesis gas fermentation. ACS Synth. Biol. 8, 2270–2279. https://doi.org/10.1021/acssynbio.9b00033.